

Optimizing Doppler laser cooling protocols for quantum sensing with 3D ion crystals in a Penning trap

John Zaris*

Department of Physics, University of Colorado, Boulder, Colorado 80309, USA

Wes Johnson

*Department of Physics, University of Colorado, Boulder, Colorado 80309, USA and
Sandia National Laboratories, Albuquerque, New Mexico, 87185, USA*

Athreya Shankar

*Department of Physics, Indian Institute of Technology Madras, Chennai, India, 600036 and
Center for Quantum Information, Communication and Computing,
Indian Institute of Technology Madras, Chennai 600036, India*

John J. Bollinger and Allison L. Carter

National Institute of Standards and Technology, Boulder, Colorado 80309, USA

Daniel H.E. Dubin

Department of Physics, University of California, San Diego, California 92093, USA

Scott E. Parker

*Department of Physics, University of Colorado, Boulder, Colorado 80309, USA and
Renewable and Sustainable Energy Institute, University of Colorado, Boulder, Colorado 80309, USA*

(Dated: February 27, 2026)

Large, 3D trapped ion crystals offer improved sensitivity in quantum sensing protocols, and are expected to be implemented as platforms in near-future experiments. However, numerical techniques used to study the laser cooling of such crystals are inefficient as the number of ions, N , in the crystal increases. Here we develop a powerful numerical framework to simulate laser cooling of up to 10^5 ions stored in a Penning trap. We apply this framework to characterize and optimize the cooling of ellipsoidal 3D crystals. We document new pathways to enhanced cooling based on the addition of an axial component to the potential energy-dominated $\mathbf{E} \times \mathbf{B}$ modes. Furthermore, we observe greatly enhanced cooling of the perpendicular kinetic energy to below 1 mK in prolate ion crystals, enabling a simplified cooling beam setup for such crystals. We propose specific values of trap and laser beam parameters which lead to optimal cooling in a variety of examples. This work illustrates the feasibility of preparing large 3D crystals for high-sensitivity quantum science protocols, motivating their use in future experiments.

I. INTRODUCTION

Trapped ion crystals are key platforms in modern quantum science research, owing to the precise control which modern experiments exert over their internal and motional degrees of freedom. In the last decade or so, much experimental work has been devoted to studying the use of two-dimensional (2D) ion crystals in Penning traps for quantum simulation and sensing applications. In particular, 2D crystals have been utilized to study quantum many-body physics [1–6], growth of entanglement in interacting systems [7, 8], creation of many-ion spin squeezed states [9, 10], and quantum sensing of motion and electric fields [11–14]. Experimental methods with single plane crystals in Penning traps continue to advance, recently allowing for site-resolved single-shot detection [15] and single-site addressing of ions [16]. While

the Penning trap has historically been the preferred apparatus for storing large 2D crystals, new experimental setups have successfully trapped 2D crystals with hundreds of ions in radiofrequency traps [17, 18], where single-site addressing is straightforward.

Currently, there is significant interest in extending experimental protocols to three-dimensional (3D) crystals with large numbers of ions. The use of 3D crystals would allow for the simulation of new many-body Hamiltonians [19], development of novel metrological applications [20, 21], and measurement of increasingly weak signals in quantum sensing experiments [13]. For example, due to the $1/\sqrt{N}$ sensitivity scaling of quantum sensing protocols, a 3D crystal with $N = 10^6$ ions could lead to a 100-fold improvement over current measurements with 2D crystals of $N \approx 100$ ions. While the equilibrium structure and laser cooling of large 3D trapped ion crystals have been studied for decades [22–25], modern methods of control and readout could now help to realize their potential in quantum science research.

* Contact author: john.zaris@colorado.edu

To utilize their quantum properties, trapped ion crystals must first be laser-cooled to ultracold temperatures. For instance, a traveling-wave potential can produce an optical dipole force (ODF) Hamiltonian which couples the internal state of the ions and their positions, as long as the ions are localized with positional fluctuations small compared to the ODF wavelength. This is known as Lamb-Dicke confinement and is a requirement for many quantum protocols. Laser cooling of 2D ion crystals in Penning traps is well-studied and has seen key improvements in recent years. Significant effort has been dedicated, in particular, to improving the cooling of the axial, or ‘drumhead’ modes, which describe ion motion perpendicular to the plane of the crystal and which are typically utilized in quantum sensing and simulation experiments. Notably, near-ground state cooling of the drumhead mode branch has been achieved by implementing electromagnetically-induced transparency (EIT) cooling, which is expected to improve quantum sensing capabilities [17, 26]. On the other hand, the potential-energy dominated $\mathbf{E} \times \mathbf{B}$ modes have proven difficult to cool, leading to unwanted broadening of the drumhead modes [27]. In fact, this is one of several problems in the study of ion crystal laser cooling for which numerical methods have proven invaluable. Novel techniques for improved $\mathbf{E} \times \mathbf{B}$ cooling have recently been proposed, and evaluated via molecular dynamics (MD) laser cooling simulations [28, 29].

The cooling dynamics of 3D crystals remain largely uncharacterized, both experimentally and theoretically. Past experimental studies have observed crystallization in spheroidal crystals [22, 23, 30], but cooling to the level of several mK has not been well-characterized. Furthermore, current numerical laser cooling simulations [31, 32] are challenging with more than a few thousand ions, as the computation of Coulomb interactions becomes intractable due to their N^2 scaling. To enable the simulations of large 3D crystals, we recently implemented an efficient, compiled code which utilizes the fast multipole method (FMM) to accelerate the calculation of Coulomb interactions between ions [33].

In this paper, we numerically study the laser cooling of 3D ion crystals in a Penning trap using our MD code. In Section II, we review the relevant Penning trap physics and introduce the MD code, including our laser cooling model. Furthermore, we describe the normal mode analysis typically used to study the excitation of ion crystals. In Section III, we examine the cooling of low-frequency, potential energy dominated $\mathbf{E} \times \mathbf{B}$ modes. In 2D crystals, these have proven difficult to cool as they experience limited coupling to the cooling lasers. However, $\mathbf{E} \times \mathbf{B}$ modes in 3D crystals include both planar and axial components, and we show that this can lead to efficient potential energy cooling. We then study the effect of several trap and laser beam parameters on the potential energy of 3D crystals. In Section IV, we demonstrate enhanced cooling of the kinetic energy in prolate 3D crystals. We discover a regime in which coupling between the axial

and planar motion allows for efficient cooling with the use of a single laser beam directed parallel to the magnetic field. Finally, in Section V, we describe numerical methods used to scale up our simulations to larger crystals and present cooling results for a $N = 10^5$ ion crystal.

II. THEORETICAL FRAMEWORK

A. Molecular Dynamics Simulation

In a Penning trap, ions are confined by a combination of static electric and magnetic fields. By applying a voltage difference between the endcap and middle electrodes such that the endcaps are at a higher potential, a positively charged ion is subject to a confining potential in the axial (\hat{z}) direction. Near the center of the trap, this potential is approximately harmonic and parameterized by

$$\phi_{trap}(\mathbf{x}) = \frac{1}{4}k_z(2z^2 - x^2 - y^2), \quad (1)$$

where $\mathbf{x} = x\hat{x} + y\hat{y} + z\hat{z}$ is the position of the ion and k_z parameterizes the strength of the potential. The axial trapping frequency is given by $\omega_z = \sqrt{qk_z/m}$, where m is the ion’s mass and q is its charge. This is the frequency of the axial center-of-mass (COM) mode of a trapped ion crystal. The potential ϕ_{trap} is deconfining in the radial direction, so an axial magnetic field, $\mathbf{B} = B\hat{z}$, is used to produce radial confinement. In the remainder of this work, we refer to motion in the plane perpendicular to \mathbf{B} as ‘planar’, ‘perpendicular’, or ‘radial’.

In order to control the global rotation frequency of an ion crystal, it is common to introduce a time-varying rotating wall potential given by

$$\phi_{wall}(\mathbf{x}, t) = \frac{1}{2}k_z\delta(x^2 + y^2)\cos[2(\varphi + \omega_r t)], \quad (2)$$

where δ parameterizes the strength of the rotating wall in relation to the trap potential, φ is the azimuthal coordinate of the ion, and ω_r is the rotating wall frequency. For an N -ion crystal, the total potential energy is given by

$$E_{pot} = \sum_{i=1}^N \left[q_i \left(\phi_{trap}(\mathbf{x}_i) + \phi_{wall}(\mathbf{x}_i, t) + \frac{1}{8\pi\epsilon_0} \sum_{j=1, j \neq i}^N \frac{q_j}{|\mathbf{x}_i - \mathbf{x}_j|} \right) \right]. \quad (3)$$

In order to study the laser cooling of 3D ion crystals in a Penning trap, we use a previously developed MD simulation framework which has been carefully benchmarked and optimized to efficiently simulate large crystals [33]. Our MD simulation evolves ions according

to the fields listed above. It utilizes the fast multipole method (FMM), via the FMM3D library [34–36], to accelerate the calculation of Coulomb interactions. Briefly, the FMM forms groups of nearby ions at different levels of refinement and calculates their multipole expansions to approximate the electric field at the locations of more distant ions. This avoids the explicit calculation of the Coulomb interaction between each pair of ions. For large ion number N , the number of FMM calculations required to find the Coulomb force on all ions scales with N , much better than the N^2 scaling of the direct Coulomb calculation. Previous benchmarking studies have characterized differences in ion crystal dynamics when the FMM is used in place of the direct Coulomb calculation [33]. While the trajectories of individual ions are not reproduced, bulk properties of the crystal, such as its energy, agree to high precision.

In the NIST Penning trap experiment modeled in this work, ${}^9\text{Be}^+$ ions are Doppler cooled using laser beams tuned near the $2s\ {}^2S_{1/2} \rightarrow 2p\ {}^2P_{3/2}$ cycling transition. An axial beam, whose intensity is low (to prevent recoil heating in the radial directions) and approximated to be uniform across the crystal, cools the ion motion parallel to \mathbf{B} . We note that the NIST experiment uses only a single axial beam. However, we use two counterpropagating axial beams, denoted by \parallel_1 and \parallel_2 , in our simulations to prevent heating of the axial COM mode when the beams are turned off. A perpendicular beam, with a higher peak intensity and smaller waist, and which is offset from the trap center by distance d , is used to cool the perpendicular motion. The beam's intensity is assumed to be Gaussian and parameterized as $I_{\perp}(\mathbf{x}) = I_{\perp,0} \exp\left(\frac{-2(y-d)^2}{w_y^2}\right) \exp\left(\frac{-2z^2}{w_z^2}\right)$, where $I_{\perp,0}$ is the central intensity and w_y (w_z) is the beam waist in the \hat{y} (\hat{z}) direction. The Doppler cooling setup is illustrated in Fig. 1. It is useful to define the saturation parameter of each beam $l \in \{\parallel_1, \parallel_2, \perp\}$ in terms of its intensity $I_l(\mathbf{x})$ as $S_l(\mathbf{x}) = I_l(\mathbf{x})\sigma_0/\hbar\omega_0\gamma_0$, where σ_0 is the scattering cross section on resonance, ω_0 is the cooling transition frequency, and $\gamma_0 = 2\pi \times 18$ MHz is the natural linewidth of the cooling transition. Note that the saturation parameters of the axial beams are uniform in space. Then, the theoretical rate at which an ion with position \mathbf{x} and velocity \mathbf{v} scatters photons from laser beam l is approximately given by [23]

$$\gamma_l(\mathbf{x}, \mathbf{v}) = S_l(\mathbf{x})\gamma_0 \frac{(\gamma_0/2)^2}{(\gamma_0/2)^2(1 + 2S_l(\mathbf{x})) + (\Delta_l - \mathbf{k}_l \cdot \mathbf{v})^2}, \quad (4)$$

where Δ_l is the detuning of the laser beam from the transition and \mathbf{k}_l is the beam's wavevector. In Eq. (4), we ignore the shift in Δ_l due to the recoil term, which is small. Throughout this work, we assume that the saturation parameter at maximum laser intensity for the axial and perpendicular beams are given by $S_{0,\parallel_1} = S_{0,\parallel_2} = 5 \times 10^{-3}$ and $S_{0,\perp} = 0.5$, respectively.

The laser cooling model implemented in our code treats

the scattering of photons by a given ion as a Poisson process [31]. Therefore, the number of photons from laser beam l scattered by ion i during a given timestep of duration Δt is computed by randomly sampling from a Poisson distribution with mean value $\gamma_l(\mathbf{x}_i, \mathbf{v}_i)\Delta t$. Each photon is absorbed along the direction of the beam's \mathbf{k} -vector, while the direction of the emitted photons is randomized and the ions' velocities are modified accordingly. This algorithm makes use of certain key simplifications. First, we approximate the time between photon absorption and emission as infinitesimal, and apply only a single momentum kick to an ion per timestep. The validity of this assumption rests on the condition $\omega_c/\gamma_0 \ll 1$, where $\omega_c = qB/m$ is the cyclotron frequency of an ion (for the NIST parameter values used here, $\omega_c/\gamma_0 \sim 0.4$). Additionally, when computing the total change in momentum of an ion, we independently calculate the momentum kick due to each laser beam. This method ignores changes in the saturation parameter for ions illuminated by multiple beams as well as interference between the counterpropagating axial beams, which would produce a standing wave in the axial direction. As mentioned, the use of two axial beams is a numerical tool and the NIST experiment uses only a single axial beam, so no standing wave exists, in practice. Finally, we ignore correlations between scattering events, which is allowable since the average number of photons scattered by a given ion during a single timestep is $\ll 1$.

Our code advances the ion motion using a cyclotronic integrator, which is a second-order, symplectic method. We use a timestep of $\Delta t = 1$ ns in this work, which is sufficiently small to satisfy the scattering condition and also to resolve the highest frequency ion motion. More details on this algorithm can be found in [31, 33]. In the following sections, we study how 3D crystal Doppler laser cooling results depend on various laser beam parameters. While the axial beams are typically very effective at cooling the axial motion to near the Doppler limit ($T_{\text{Doppler}} = \hbar\gamma_0/2k_B$), the cooling of the perpendicular motion is highly sensitive to the perpendicular beam's parameters, including its waist, detuning, and offset from the origin.

B. Ion crystal normal modes

Ion motion in an ultracold crystal is described by the crystal's normal modes. This treatment is valid as long as the ion crystal remains near its equilibrium configuration. The method of computing normal modes of various trapped ion configurations is described in many papers [19, 27, 37–39]. We will provide a brief description of the analysis for a general 3D crystal here. We introduce the state vector,

$$|q\rangle = \begin{pmatrix} |\delta x\rangle \\ |v\rangle \end{pmatrix}, \quad (5)$$

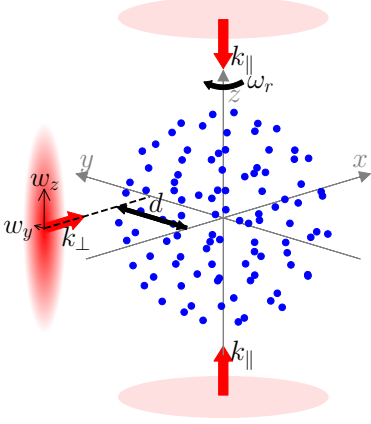


FIG. 1: The setup to cool the crystal relies on two axial and one perpendicular cooling beam. The axial beams have a low intensity which we approximate as uniform across the crystal in our simulations. They are detuned by $\Delta_{\parallel 1} = \Delta_{\parallel 2} = -\gamma_0/2$ from resonance with the $2s^2S_{1/2} \rightarrow 2p^2P_{3/2}$ transition. The perpendicular beam is offset from the trap center by a distance d and has detuning Δ_{\perp} . Unlike in the case of a 2D crystal, here, the perpendicular beam waist in both directions, w_y and w_z , affect the cooling rate. Figure is reproduced from [33].

which has length $6N$ and contains the positions and velocities of the ions in the crystal. After expanding the system Lagrangian about equilibrium and computing the Euler-Lagrange equations of motion, one obtains

$$\frac{d|q\rangle}{dt} = \begin{pmatrix} \mathbb{O}_{3N} & \mathbb{1}_{3N} \\ -\mathbb{K}/m & -2\mathbb{W}/m \end{pmatrix} |q\rangle \equiv \mathbb{D} |q\rangle. \quad (6)$$

Each of the submatrices above has size $3N \times 3N$. The matrix \mathbb{K} is known as the stiffness matrix and is real and symmetric. The effect of the Lorentz force is encapsulated in the real, antisymmetric matrix \mathbb{W} . The exact forms of \mathbb{K} and \mathbb{W} are provided in [33]. Diagonalizing this system produces $3N$ normal modes $|u_n\rangle$ with frequencies ω_n such that the time evolution of the state vector can be expressed as

$$|q\rangle = \sum_{n=1}^{3N} [A_n e^{-i\omega_n t} |u_n\rangle + A_n^* e^{i\omega_n t} |u_n^*\rangle], \quad (7)$$

where A_n is the complex amplitude of mode n and $|u_n^*\rangle$ is the complex conjugate of $|u_n\rangle$. Each $6N$ dimensional eigenmode includes $3N$ position amplitudes and $3N$ velocity amplitudes, which describe the motion of every ion in each spatial direction. To refer to various components of the eigenvectors, it is often convenient to write $|u_n\rangle = (|u_n^r\rangle, |u_n^v\rangle)^T$, where $|u_n^r\rangle = (|u_n^x\rangle, |u_n^y\rangle, |u_n^z\rangle)^T$ and $|u_n^v\rangle = (|u_n^{vx}\rangle, |u_n^{vy}\rangle, |u_n^{vz}\rangle)^T$ are the position and velocity components, respectively.

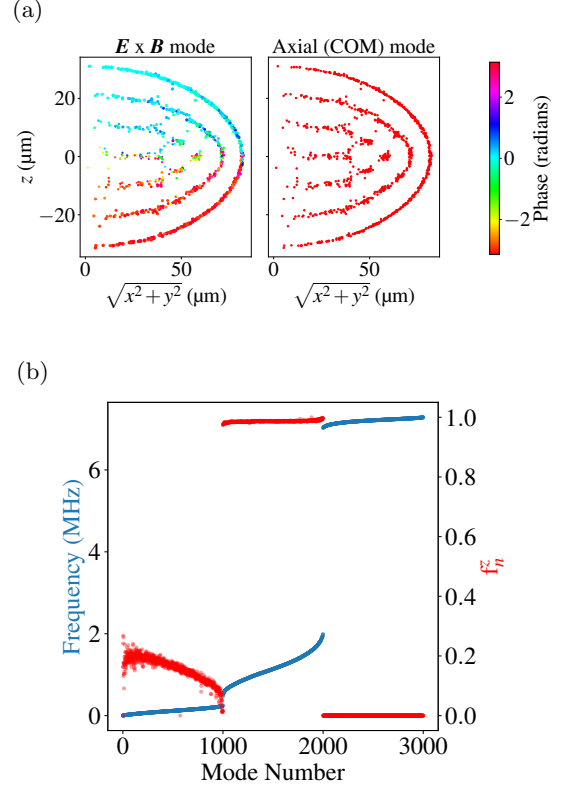


FIG. 2: (a) Two examples of 3D crystal normal modes are illustrated. The same equilibria configuration for a $N = 1000$ ion crystal is shown in each panel. The shell structure characteristic of ultracold mesoscopic crystals is evident. The relative phase of each ion in the mode is represented by its color and the relative amplitude of the ion's motion is represented by its size. The left-hand plot shows an $\mathbf{E} \times \mathbf{B}$ mode in which the ions above $z = 0$ have a nearly uniform phase and ions below $z = 0$ have a different, but also nearly uniform phase (mode 2). For this plot, the phase is calculated using $\phi_p = \arg\{u_n^x\}$, where u_n^x is the x -component of the positional part of eigenmode n . The right-hand panel illustrates the axial center of mass mode (mode 1884), in which all ions move in phase at frequency ω_z . Here, the phase is $\phi_p = \arg\{u_n^z\}$. (b) The normal mode frequencies for the crystal shown in (a) are plotted in blue. The mode branches occupy distinct frequency bands and are separated by frequency gaps, as is seen in 2D crystals. In order of increasing frequency, they are the $\mathbf{E} \times \mathbf{B}$, axial, and cyclotron branches. In more prolate 3D crystals, the gap between branches can vanish. The axial component of each mode, f_n^z , is shown in red. It is computed using Eq. 8. The $\mathbf{E} \times \mathbf{B}$ modes gain a large axial component, even in 3D crystals with moderate aspect ratios. The axial modes have a small, but noticeable, planar component in this case. Note that the axial center-of-mass mode, for which $f^z = 1$, is no longer the highest frequency mode, as is the case in 2D crystals.

Here we briefly review the general differences in the mode spectra between 2D and 3D crystals. In an N -ion 2D crystal, N normal modes describe the purely axial motion of the ions while $2N$ modes describe purely planar motion. The planar mode branches are further divided into low frequency $\mathbf{E} \times \mathbf{B}$ modes and high frequency cyclotron modes. For most trapping parameters, the three mode branches are well separated in frequency space, with axial mode frequencies located between $\mathbf{E} \times \mathbf{B}$ mode and cyclotron mode frequencies. In 3D crystals, the normal modes are no longer purely planar or axial, due to the mixing between degrees of freedom in \mathbb{K} . However, the modes still tend to form three distinct branches. We will refer to the branches in 3D crystals using the same names as before, but it is useful to keep in mind that the axial modes now have a planar component and the $\mathbf{E} \times \mathbf{B}$ and cyclotron modes have an axial component. As we will see in the next section, oblate 3D crystals generally have mode branches which are well-separated in frequency space and their modes exhibit minimal planar-axial coupling. On the other hand, prolate 3D crystals have smaller frequency gaps between branches and significant planar-axial coupling.

We illustrate the normal modes of a small oblate 3D ion crystal in Fig. 2. In Fig. 2a we show two crystal eigenvectors in which sections of the crystal move in phase. For instance, the axial COM mode is characterized by the in-phase motion of all ions. Notably, this mode is still purely axial, even in 3D crystals. In Fig. 2b, we plot the mode frequencies of the same crystal. For this set of trap parameters, the three mode branches are well-separated. Also in Fig. 2b, we plot the axial fraction of each mode, computed according to

$$f_n^z = \frac{\langle u_n^z | u_n^z \rangle}{\langle u_n^r | u_n^r \rangle}. \quad (8)$$

The $\mathbf{E} \times \mathbf{B}$ modes have a significant axial component, typical of many 3D crystals. On the other hand, in this regime, the axial modes describe nearly pure axial motion and the cyclotron modes remain almost entirely planar.

III. COOLING ACROSS THE 2D-3D TRANSITION

We begin by investigating laser cooling across the transition from a 2D crystal to a 3D crystal. This transition occurs when the ratio of the confining potential in the radial and axial directions reaches a critical value. This ratio, denoted by β , is explicitly given by

$$\beta = \frac{\omega_r(\omega_c - \omega_r)}{\omega_z^2} - \frac{1}{2}. \quad (9)$$

In the NIST Penning trap experiment, β is typically modulated by varying ω_r . In recent work with 2D trapped ion

crystals, it has proven difficult to cool the low-frequency $\mathbf{E} \times \mathbf{B}$ modes to less than a few milliKelvin. This is because Doppler laser cooling directly removes kinetic energy, but these modes are dominated by potential energy. In this section, we investigate how the mode spectrum of 3D crystals affects the potential energy temperatures achievable using Doppler laser cooling. We also characterize the kinetic energy cooling of these crystals and study the effects of several trap parameters on cooling results.

A. Simulation setup

Our laser cooling simulations proceed in three main steps. First, the equilibrium configuration of the ion crystal is found. Then, the crystal positions and velocities are perturbed such that the potential and kinetic energies are initialized at temperature T_i . Finally, the crystal is evolved in time via our MD code, which includes laser cooling.

In order to study laser cooling of 3D crystals, we simulate traps with various values of ω_r . Our first set of simulations investigates five $N = 1000$ ion crystals with $\omega_r/2\pi = 176, 178.15, 220, 400,$ and 700 kHz, respectively. The remaining trap parameters are as follows: $B = 4.4588$ T, $\omega_z = 2\pi \times 1.59$ MHz, and $\delta = 0.0104$. The equilibria of these crystals are found using the BFGS method provided by SciPy and are displayed in Fig. 3a. We briefly note that slightly lower energy local minimum configurations may be found using a variety of methods, including numerical damping and the modified basin hopping algorithm in [19]. We will discuss energy minimization techniques in more detail in Section V. The crystal equilibrium corresponding to $\omega_r = 2\pi \times 176$ kHz is found to be planar. At 178.15 kHz, the outer ions are all located at $z = 0$, but the central ions have popped out of the plane and have axial coordinates on the order of 1 micron. Further increasing the rotation frequency to 220 kHz, the equilibrium consists of several planes of ions. The number of planes decreases with the distance from the trap center since the axial extent of the crystal is largest at $r = 0$. As ω_r continues to increase, the axial extent of the crystal also grows. At $\omega_r = 2\pi \times 400$ and $2\pi \times 700$ kHz, the equilibria consist of concentric ellipsoidal shells of ions, which are less defined near the trap center.

The frequency spectra of these crystals are displayed in Fig. 3b. In the majority of trap parameter space, 2D crystals exhibit large frequency gaps, typically on the order of 1 MHz, between the highest frequency $\mathbf{E} \times \mathbf{B}$ mode and the lowest frequency axial mode. The gap disappears near $\omega_r = 2\pi \times 178.15$ kHz because the 2D to 3D transition that occurs at this rotation frequency is a buckling transition of second order: the planar lattice becomes unstable due to an axial mode that approaches zero frequency as ω_r increases toward the transition value [40]. As the frequency gap vanishes, resonant mode coupling

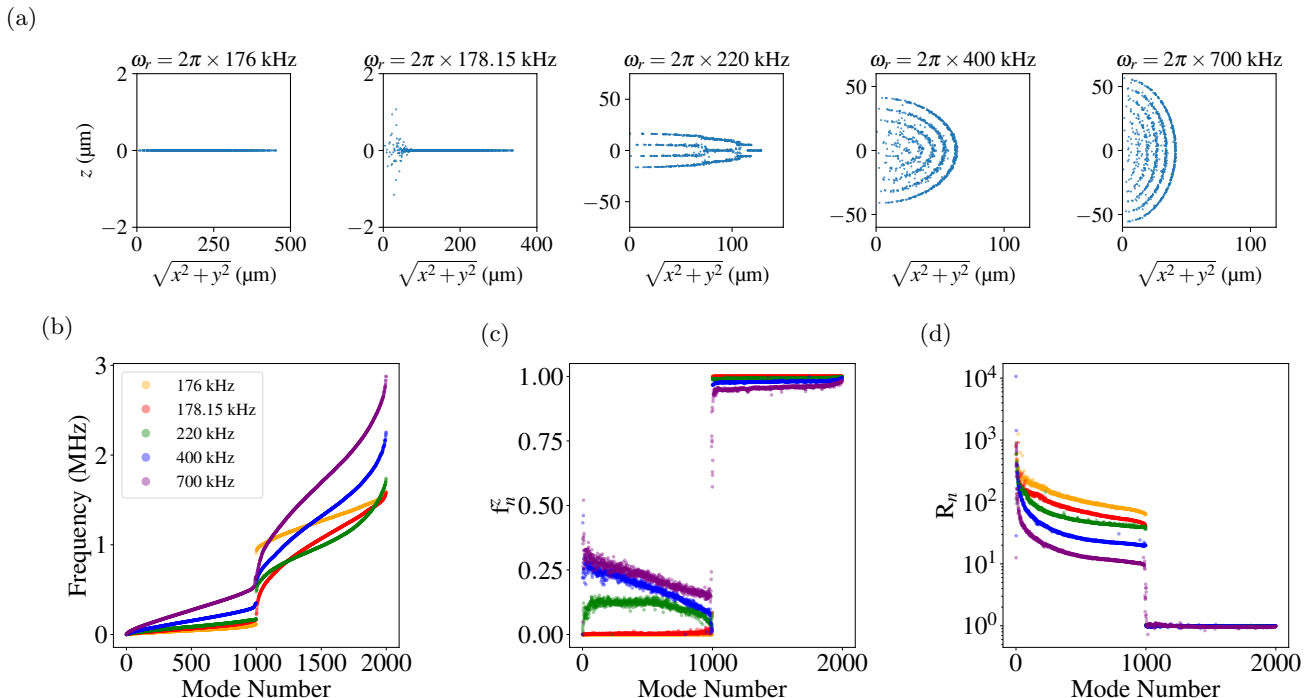


FIG. 3: (a) The shape of $N = 1000$ ion crystals are plotted for different values of ω_r . The equilibrium configurations plotted correspond to the following trap parameters: $B_z = 4.4588$ T, $\omega_z = 2\pi \times 1.59$ MHz, $\delta = 0.0104$. The transition from a 2D crystal to a 3D crystal occurs near $\omega_r = 2\pi \times 178.15$ kHz. The equilibrium crystal corresponding to this frequency is nearly 2D, except the most central ions have popped out of the plane and have axial coordinates of up to ~ 1 μm . As ω_r is increased further, the axial extent of the crystal increases and the shell structure becomes evident. (b) The $\mathbf{E} \times \mathbf{B}$ (mode numbers 1-1000) and axial (mode numbers 1001-2000) normal mode frequencies are plotted for the ion crystals in (a). Most 2D crystals have $\mathbf{E} \times \mathbf{B}$, axial, and cyclotron modes which occupy distinct frequency bands (orange curve). However, near the 2D-3D transition, the highest frequency $\mathbf{E} \times \mathbf{B}$ and lowest frequency axial modes approach one another (red curve). The frequency gap reappears immediately after the transition, but again vanishes as ω_r continues to increase. Therefore, resonant mode coupling in large β 3D crystals may result in enhanced Doppler laser cooling. (c) The axial component of the $\mathbf{E} \times \mathbf{B}$ and axial modes is shown for each of the crystals. As ω_r increases, $\mathbf{E} \times \mathbf{B}$ modes gain larger axial components and axial modes gain a larger planar component. The $\mathbf{E} \times \mathbf{B}$ modes of 3D crystals may, therefore, be cooled by the axial beams in the NIST setup. (d) The potential energy fraction of the $\mathbf{E} \times \mathbf{B}$ and axial modes. For crystals with larger ω_r , the $\mathbf{E} \times \mathbf{B}$ modes have a larger kinetic energy component. Since Doppler laser cooling directly reduces the kinetic energy, this may result in enhanced cooling of large β crystals.

between branches is expected to produce enhanced cooling of the $\mathbf{E} \times \mathbf{B}$ modes [28]. For ω_r above the 2D to 3D transition value, the gap opens up again because the stable 3D equilibrium is characterized by axial modes which have a finite (that is, minimum) frequency. However, in these crystals, individual modes experience mixing between the axial and planar degrees of freedom, as shown in Fig. 3c. Note that the $\mathbf{E} \times \mathbf{B}$ modes in the 3D crystals have large values of f^z , or significant axial components.

When ω_r is well above the transition value, the simulations observe that the frequency gap closes again. This can be understood by comparing the maximum frequency of $\mathbf{E} \times \mathbf{B}$ modes with the minimum frequency of axial modes in a plasma spheroid. When the plasma is a spheroid, the maximum frequency $\omega_{E_{max}}$ of $\mathbf{E} \times \mathbf{B}$

modes is roughly

$$\omega_{E_{max}} \approx \frac{\omega_p^2}{2\Omega_v}, \quad (10)$$

where $\Omega_v \equiv \omega_c - 2\omega_r$ is the vortex frequency, the effective cyclotron frequency in the rotating frame of the plasma, and ω_p is the ion plasma frequency, given in terms of the plasma rotation frequency by

$$\omega_p^2 = 2\omega_r(\omega_c - \omega_r). \quad (11)$$

Eq. (10) follows by considering the large wavenumber and large vortex frequency limit of the dispersion relation [41] for plasma waves in a magnetized spheroid. For an ion crystal it is only a rough estimate because correlation effects affect the restoring forces.

The minimum frequency $\omega_{\parallel min}$ of the axial modes in a plasma spheroid can also be roughly estimated, from the dispersion relation for magnetized plasma waves in a uniform plasma [42],

$$\omega^2 = \omega_p^2 \frac{\tilde{k}_z^2}{\tilde{k}_\perp^2 + \tilde{k}_z^2}, \quad (12)$$

where \tilde{k}_z and \tilde{k}_\perp are the axial and perpendicular wave numbers respectively (with respect to the magnetic field direction). The wave numbers are quantized by the finite size of the plasma, with values that may be estimated as $\tilde{k}_z \approx m_z \pi / (2Z)$ and $\tilde{k}_\perp \approx m_\perp \pi / R$ where R is the radius of the plasma, Z is its axial half-length, and m_z and m_\perp are positive integers. This approximate theory breaks down in the 2D regime where Z is zero, but provides order of magnitude estimates for normal mode frequencies when $Z > a$, where a is the inter-ion spacing (Wigner-Seitz radius). Also, the integers m_z and m_\perp cannot be arbitrarily large, since the theory is only sensible for inverse wave numbers less than of order a . The lowest frequency axial modes then have the smallest possible \tilde{k}_z , of order $1/Z$, and the largest possible \tilde{k}_\perp , of order $1/a$, yielding a minimum axial frequency of roughly

$$\omega_{\parallel min} \approx C \omega_p \frac{a}{Z} \quad (13)$$

where C is a constant of order unity. The value of C can be estimated by comparing Eq. (13) to simulation results, which gives $C \approx 2$. Eqs. (10) and (13) are plotted in Fig. 4 versus the plasma rotation frequency and compared to the simulation results for the crystals shown in Fig. 3. For the simulated crystals with $176 \text{ kHz} \leq \omega_r / 2\pi \leq 400 \text{ kHz}$, the $\mathbf{E} \times \mathbf{B}$ modes are the N lowest frequency modes while the axial modes are the N middle frequency modes. Therefore, when the modes are listed in order of increasing frequency ω_{Emax} and $\omega_{\parallel min}$ are the frequencies of modes N and $N + 1$, respectively. However, for the $\omega_r = 700 \text{ kHz}$ crystal, the lowest frequency N modes no longer correspond exactly to the $\mathbf{E} \times \mathbf{B}$ modes, which we define as the N modes with the largest values of R_n . In this case, we find that ω_{Emax} and $\omega_{\parallel min}$ are the frequencies of mode numbers 1003 and 995, respectively. For a plasma of $N = 1000$ ions, Fig. 4 shows how the frequency gap disappears as the maximum $\mathbf{E} \times \mathbf{B}$ frequency increases and the minimum axial frequency decreases.

Having determined the crystal equilibria, we next initialize the crystals at $T_i = 10 \text{ mK}$. To initialize the kinetic energy, the ions are randomly assigned initial velocities, v , according to the Maxwell-Boltzmann distribution,

$$f(v) = \left(\frac{m}{2\pi k_B T_i} \right)^{3/2} \exp \left(- \frac{mv^2}{2k_B T_i} \right), \quad (14)$$

where k_B is the Boltzmann constant. Since the $\mathbf{E} \times \mathbf{B}$ modes are dominated by potential energy, they are not

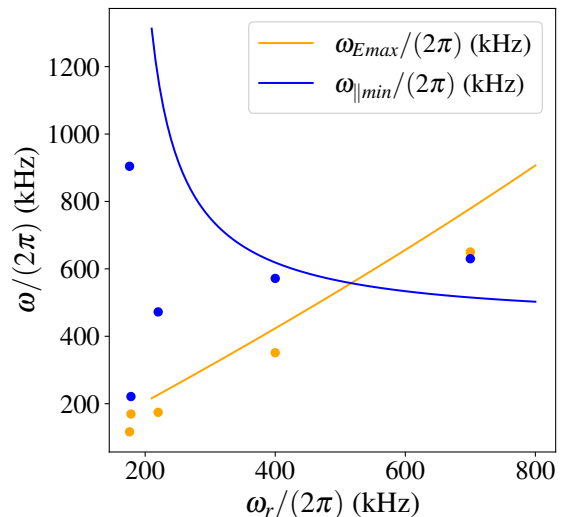


FIG. 4: Theory estimates for the maximum $\mathbf{E} \times \mathbf{B}$ mode frequency and the minimum axial frequency versus plasma rotation frequency are shown in orange and blue curves, respectively. These plots are obtained using Eq. (10) and Eq. (13). The theoretical treatment predicts that $\omega_{\parallel min} > \omega_{Emax}$ for $\omega_r \lesssim 500 \text{ kHz}$. For larger values of ω_r , $\omega_{\parallel min}$ becomes smaller than ω_{Emax} . This behavior is observed in the mode frequencies of the crystals from Fig. 3, which we plot here using orange and blue dots. Note that the difference $\omega_{\parallel min} - \omega_{Emax}$ nearly vanishes in the simulation data from $\omega_r = 178.15 \text{ kHz}$. This occurs near the 2D to 3D transition. The theory plots do not account for this behavior, but this effect is well-understood (see text).

excited by initializing the ion velocities. Instead, the potential energy is independently initialized using the Metropolis-Hastings algorithm to perturb the ion positions [27]. Starting from equilibrium, a given ion is displaced in a random direction by distance $\text{rand}(0, \delta x)$. In this work we choose $\delta x = 0.5 \mu\text{m}$. The energy before and after the change in the ion's position are denoted E_0 and E_{new} , respectively, and the list of ion coordinates are $\{\mathbf{x}_0^n\}$ and $\{\mathbf{x}_{new}^n\}$. The MH algorithm accepts this change in the ion's position if $E_{new} < E_0$, or if $\text{rand}(0, 1) < \exp[-(E_{new} - E_0)/k_B T_i]$. In this case, we set $\{\mathbf{x}_0^n\} = \{\mathbf{x}_{new}^n\}$ and $E_0 = E_{new}$. Otherwise, the displacement is rejected. Then, the next ion in the crystal is randomly displaced and this process is repeated for each ion, constituting one full scan of the MH algorithm. We complete on the order of 1000 scans in order to initialize the potential energy of the crystal at T_i .

After the crystal is initialized at T_i , it is evolved in time using our MD code, allowing us to study the laser cooling of an ion crystal for a given set of laser and trap parameters.

B. Potential energy cooling

Since $\mathbf{E} \times \mathbf{B}$ modes contain mostly potential energy, they have proven difficult to cool in the case of 2D crystals [28]. We now study the reduction in potential energy, or potential energy cooling, experienced by the 3D crystals in Fig. 3 during Doppler laser cooling. Prior to discussing laser cooling simulations, we identify several factors which may lead to efficient potential energy cooling in 3D crystals, thereby motivating this investigation.

First, as seen in Fig. 3c, the $\mathbf{E} \times \mathbf{B}$ modes of 3D crystals have large axial components, f^z . This coupling between perpendicular and axial degrees of freedom in 3D crystal modes, which we will refer to as ‘ f^z -coupling’, may result in efficient $\mathbf{E} \times \mathbf{B}$ mode cooling. Because axial motion is efficiently cooled by the axial laser beams, the planar component of the $\mathbf{E} \times \mathbf{B}$ modes in 3D crystals may experience significant direct cooling. However, this reasoning is further complicated by the consideration that the $\mathbf{E} \times \mathbf{B}$ modes are dominated by potential energy. This fact is illustrated in Fig. 3d, where we plot the ratio, R_n , of potential energy to kinetic energy in each normal mode, given by

$$R_n = \frac{\langle u_n^r | \mathbb{K} | u_n^r \rangle}{m \langle u_n^v | u_n^v \rangle}. \quad (15)$$

Since Doppler laser cooling primarily cools kinetic energy, the efficiency with which the axial beams can cool the axial component of the $\mathbf{E} \times \mathbf{B}$ modes may be limited.

Crystals with larger values of β may also see enhanced potential energy cooling due to ‘resonant mode coupling’ between the $\mathbf{E} \times \mathbf{B}$ and axial modes. In the case of 2D crystals, it has been shown that when the frequency gap between these branches closes, the $\mathbf{E} \times \mathbf{B}$ modes are sympathetically cooled as energy is removed from the axial modes [28]. As illustrated in Fig. 3b, the frequency gap vanishes in 3D crystals as ω_r is increased. At $\omega_r = 2\pi \times 700$ kHz, the gap is no longer visible.

MD laser cooling simulations inherently include f^z -coupling and resonant mode coupling and, therefore, can elucidate the effects of trap and laser beam parameters on the attainable ion crystal temperatures. Our first set of cooling simulations compares the potential energy cooling of the crystals shown in Fig. 3. The values of the trap parameters used in these simulations are listed in the previous section. The laser parameters are as follows: $w_y = 20\sqrt{2}$ μm , $w_z = 100\sqrt{2}$ μm , $\Delta_{\parallel} = -\gamma_0/2$, $S_{\parallel} = 0.005$, $S_{\perp} = 0.5$. For each crystal, we have run simulations with a variety of values for Δ_{\perp} and d , which are relatively easy to tune experimentally. The exact values used in the parameter scans are different for each crystal, as we use the theory developed in [43] to choose ranges which result in optimal kinetic energy cooling. We expect to achieve the best potential energy cooling in a similar parameter space [33]. The cooling of the potential energy due to the perpendicular and axial Doppler cooling beams is simulated for 16 ms and is shown in Fig. 5. For

clarity, we only plot the cooling results for the (Δ_{\perp}, d) pair which results in the best potential energy cooling for each crystal. The exact values are listed in Table I. However, we note that the potential energy is quite similar for a variety of (Δ_{\perp}, d) pairs near the optimal values. The temperature corresponding to the potential energy of an ion crystal $\{\mathbf{x}_i(t)\}_{i=1}^N$, at time t , is calculated using

$$T^{PE}(t) = \frac{2}{3} \frac{\sum_{i=1}^N (E_{pot}(\mathbf{x}_i(t)) - E_{pot}(\mathbf{x}_i^0))}{Nk_b}, \quad (16)$$

where \mathbf{x}_i^0 is the equilibrium ion configuration. Here, we subtract the equilibrium potential energy, $E_{pot}(\mathbf{x}_i^0)$, from the total potential energy before dividing by the factor Nk_b to convert to units of temperature. The factor of $2/3$ accounts for the fact that the potential energy is shared (not necessarily equally) between three spatial degrees of freedom. We note that, in some cases with highly effective laser cooling, the potential energy of the ion crystal after simulated cooling is lower than the equilibrium potential energy found in our initialization process using the SciPy library. This behavior is a result of the complicated energy landscape of 3D crystals, which includes many local energy minimum states. In order to ensure that our potential energy values are positive, we perform another SciPy minimization following the laser cooling simulations. The configuration generated by this final energy minimization is then what we define as $\{\mathbf{x}_i^0\}$.

We run simulations using two different values of δ ($\delta = 0.0104$ and $\delta = 0.104$), and begin by discussing the results of the small δ case. For the crystal with the smallest β (or ω_r), the potential energy quickly cools to ~ 7 mK, but further cooling proceeds at a prohibitively slow rate. Increasing β to near the 2D-3D transition, significantly enhanced potential energy cooling is observed, consistent with the results from [28]. We note that this is a regime which is uniquely well-suited to laser cooling of 2D crystals. For crystals with slightly smaller or slightly larger values of β , Doppler laser cooling of the potential energy becomes markedly less effective. Observing the cooling of the $\omega_r = 2\pi \times 220$ kHz crystal, it appears

TABLE I: The values of perpendicular laser beam parameters Δ_{\perp} and d used in the simulations shown in Fig. 5 are listed here. As explained in the text, these values result in optimal potential energy cooling for the respective crystal.

$\omega_r/2\pi$ (kHz)	δ	$\Delta_{\perp}/2\pi$ (MHz)	d (μm)
176	0.0104	-50	8.2
178.15	0.0104	-150	5.8
220	0.0104	-75	1.0
220	0.104	-75	13.0
400	0.0104	-20	20.2
400	0.104	-55	20.2
700	0.0104	-350	10.6
700	0.104	-150	25.0

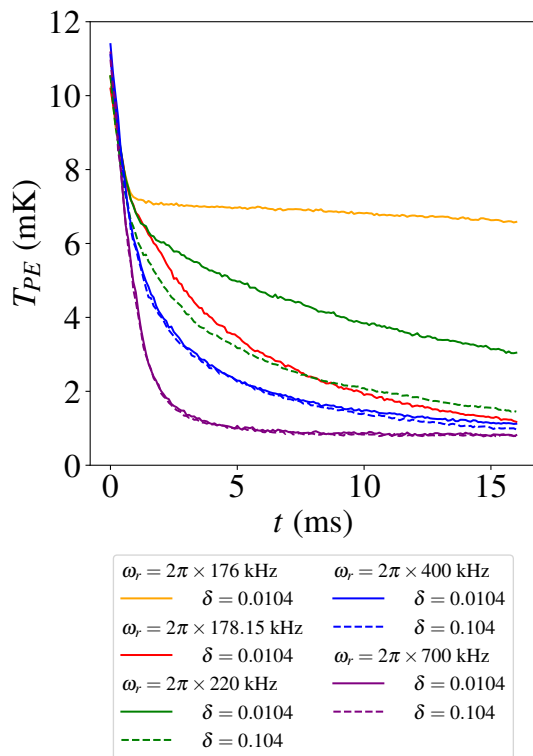


FIG. 5: The potential energy cooling is illustrated for crystals with different values of ω_r and δ . The kinetic and potential energies are initialized at 10 mK and then laser cooling is simulated for 16 ms. **Solid lines (small δ):** The potential energy of 2D crystals is generally difficult to cool, as shown by the yellow curve. By tuning the trap parameters such that the crystal is near the 2D-3D transition, the potential energy can be cooled efficiently (red curve). After the transition, an oblate 3D crystal is produced and, again, the potential energy cools relatively slowly (green curve). By further increasing β , a combination of the increased axial component of the $\mathbf{E} \times \mathbf{B}$ modes and a reduced gap between mode branches leads to enhanced cooling (blue and purple curves). **Dashed lines (large δ):** Increasing the strength of the rotating wall potential, δ , can reduce the potential energy of 3D crystals. This is seen most dramatically in the case of the $\omega_r = 2\pi \times 220$ kHz crystal.

that, when δ is small, low β 3D crystals suffer similar cooling obstacles as seen in 2D crystals. In particular, the potential energy quickly cools to ~ 6 mK within a few milliseconds, but then cools at a significantly slower rate. Still, the cooling is notably more effective than for the $\omega_r = 2\pi \times 176$ kHz 2D crystal. We attribute this behavior to f^z -coupling, as the $\mathbf{E} \times \mathbf{B}$ modes in this crystal have substantial f^z values. At $\omega_r = 2\pi \times 400$ kHz, the crystal's potential energy can be quickly cooled to ~ 1 mK, owing to stronger f^z -coupling. Resonant mode coupling between the $\mathbf{E} \times \mathbf{B}$ and axial mode branches seems less likely to cause this rapid cooling, as there still ex-

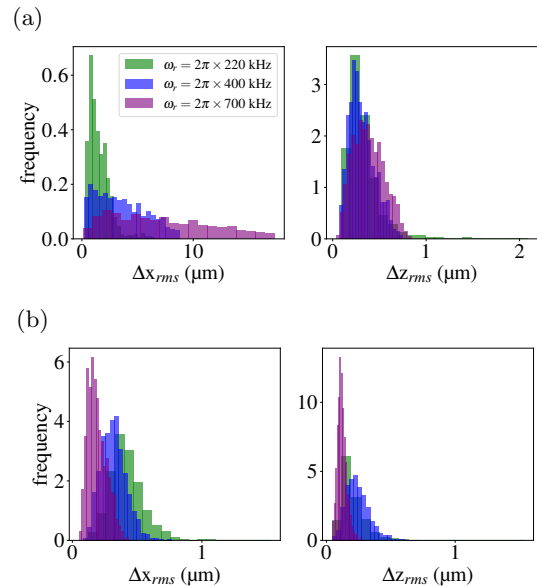


FIG. 6: The rms ion displacements during the last 1 ms of laser cooling for the three 3D crystals from Fig. 5. The upper plots show the displacements in the small δ ($\delta = 0.014$) case, while the lower plots illustrate the large δ ($\delta = 0.104$) case. Increasing the rotating wall strength significantly improves ion confinement in the perpendicular direction (here, we show the rms displacement in the \hat{x} direction). It also improves axial confinement, to a lesser extent. The $\omega_r = 2\pi \times 700$ kHz crystal exhibits the worst confinement in the small δ case, but the best confinement in the large δ case. This demonstrates that a strong rotating wall is essential when cooling large β crystals, which have smaller extent in the perpendicular directions.

ists a significant gap between branches at this value of ω_r . However, additional work is needed to definitively evaluate the relative contribution of these two effects. For instance, cooling simulations using linearized versions of the forces would eliminate mode coupling and could, therefore, be compared to our full dynamics results to help to quantify the effects of resonant coupling. Finally, at $\omega_r = 2\pi \times 700$ kHz, the potential energy is cooled even faster. In this case, resonant mode coupling may play a significant role since there is no longer a frequency gap between branches.

C. Laser torque considerations

Since ions absorb perpendicular beam photons from a single direction, but emit them in a random direction, on average the beam exerts a torque on the crystal. A sufficiently large value of δ results in a rotating wall which is strong enough to provide a restoring torque, such that the global rotation frequency of the crystal remains very

close to ω_r during laser cooling. If δ is not sufficiently large, then the laser torque can cause the ion crystal to slip in the azimuthal direction. This phenomenon, known as slip-stick dynamics, has been observed experimentally in Penning trap ion crystals [44]. Over long time scales, discrete slips of the crystal lead to the global rotation frequency to deviate from ω_r . In this section, we first study the effect of the rotating wall strength, δ , on a crystal's potential energy. Next, we analyze the effect of δ on the confinement of ions in the rotating frame.

To evaluate the effect of δ on the potential energy, we simulate laser cooling in a trap with $\delta = 0.104$ for the cases of $\omega_r/2\pi = 220, 400,$ and 700 kHz. All other parameters are held fixed, although we again test a variety of Δ_\perp and d values, and plot only the cooling results for the parameter pair which has the best potential energy cooling. These cooling results are illustrated as dotted lines in Fig. 5 and show that increasing δ can improve potential energy cooling.

To discern how well the rotating wall is able to balance the laser beam torque, it is useful to calculate the root-mean-square (rms) displacement of the ions in the frame which rotates at frequency ω_r . If the rms displacement over a duration $\tau_{rms} > 1/\omega_r$ is small compared to the inter-ion spacing, then the crystal exhibits little to no slipping out of the rotating frame. This is essential since minimizing the crystal motion in the rotating frame is key to the implementation of quantum sensing protocols. The perpendicular and axial rms displacements of ion i in the rotating frame are found using

$$\Delta\eta_{rms}^i = \sqrt{\langle |\eta_i - \langle \eta_i \rangle|^2 \rangle}, \quad (17)$$

where $\eta = x$ or z , respectively, and $\langle \rangle$ represents the time average over the last millisecond of cooling. Note that while we compute the perpendicular confinement by looking at motion along the \hat{x} direction, one could also choose the \hat{y} direction, or even both perpendicular directions.

In Fig. 6, we plot histograms of the rms displacement of the ions in the $\omega_r/2\pi \in \{220, 400, 700\}$ kHz crystals with $\delta \in \{0.0104, 0.104\}$. For the small δ case, the perpendicular displacements of the ions are relatively large, especially for larger values of ω_r , suggesting that the rotating wall potential is not strong enough to counteract the laser torque and enforce the global rotation frequency of the crystal. The perpendicular displacements are much smaller in the large δ case, meaning that the ions remain nearly fixed in the rotating frame and the crystal rotates globally at a frequency very close to ω_r . The improvement in ion confinement is most dramatic for the crystals with larger ω_r . This behavior is expected; the crystals with larger ω_r have smaller extents in the perpendicular direction, so the torque exerted by the rotating wall is smaller. Therefore, a larger value of δ is required to enforce global rotation at ω_r in such crystals. The axial displacement of ions is also smaller when using a large δ , but this effect is less dramatic because the

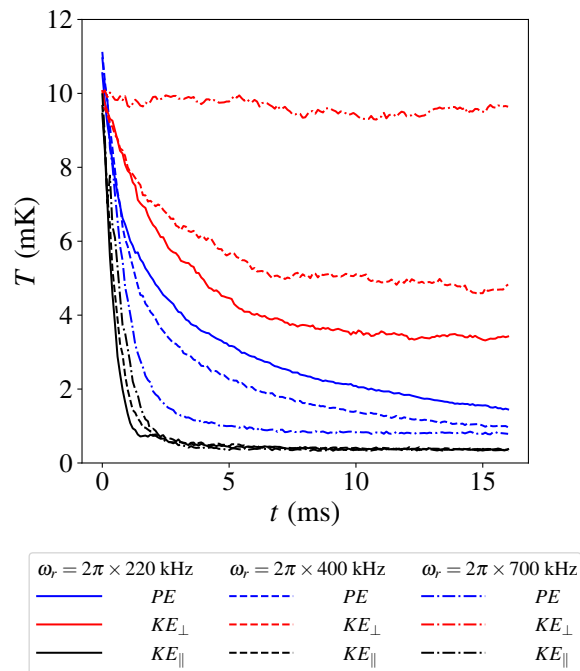


FIG. 7: The kinetic and potential energy cooling of the large δ crystals from Fig. 5. The energies are initialized at 10 mK before laser cooling is simulated. While the potential energy cooling improves as ω_r increases, the perpendicular kinetic energy cooling worsens. This behavior agrees with the kinetic energy cooling theory developed in [43]. The axial kinetic energy is well-cooled to < 1 mK in all cases.

laser torque causes perpendicular motion. Interestingly, while ion confinement in the $\omega_r = 2\pi \times 700$ kHz crystal improves significantly when δ is increased, the potential energy cooling does not change appreciably (see Fig. 5).

D. Kinetic energy cooling

While we have focused, so far, on the cooling of potential energy in 3D crystals, it is equally important to ensure that the kinetic energy is sufficiently well-cooled. For instance, in 2D crystals, excited axial modes have been shown to add noise to quantum sensing measurements [27].

In Fig. 7 we plot the kinetic energy (divided into perpendicular and axial components) as the $\delta = 0.104$ crystals from Fig. 5 are laser cooled. The potential energies are plotted again, for completeness. In all cases, the axial kinetic energy, KE_\parallel , is cooled to < 1 mK within a few milliseconds. However, the perpendicular kinetic energy, KE_\perp is not as well-cooled. The $\omega_r = 2\pi \times 220$ kHz crystal reaches the lowest KE_\perp , which is still relatively high, at ~ 4 mK. While increasing ω_r produces better PE cooling, it also leads to worse KE_\perp cooling. The higher KE_\perp is presumably due to elevated cyclotron

motion, and is consistent with theory that accounts for the dispersion of Doppler shifts across the waist of the perpendicular laser cooling beam [43]. Nevertheless, in order to prepare experimentally useful crystals, it will be important to further reduce KE_{\perp} while maintaining small potential energies.

In order to achieve this aim, we propose to reduce the perpendicular beam waist, w_y , from $20\sqrt{2} \mu\text{m}$ to $5\sqrt{2} \mu\text{m}$, while holding the peak laser intensity constant. Previous simulations showed that narrower waists often result in reduced potential and kinetic energies [33, 43]. Since it is more challenging experimentally to vary the beam waist, simulations can help determine whether there is a sufficient benefit to warrant such a change to the setup. We repeat the large δ simulations for $\omega_r/2\pi = 700$ kHz, this time setting $w_y = 5\sqrt{2} \mu\text{m}$. Changing the beam waist also changes the optimal (Δ_{\perp}, d) parameter space for kinetic energy cooling, and this is reflected in our simulations. In Fig. 8, we compare the kinetic and potential energies for crystals with $w_y = 20\sqrt{2} \mu\text{m}$ and $w_y = 5\sqrt{2} \mu\text{m}$. Here, we show the final temperatures after 16 ms of laser cooling for each (Δ_{\perp}, d) parameter pair. By reducing w_y , we find that KE_{\perp} is dramatically reduced over a large parameter space. Temperatures below 3 mK appear achievable, and even lower temperatures can likely be reached by further reducing w_y .

IV. ENHANCED COOLING IN PROLATE CRYSTALS

In the previous section, we studied crystals in which f^z -coupling led to enhanced potential energy cooling. By further increasing β , f^z -coupling can be introduced in the high frequency cyclotron mode branch. We characterize the KE_{\perp} cooling which is achievable in this regime, and find that the kinetic energy is cooled below the theoretical limits presented in [33, 43]. Furthermore, we discover a highly coupled parameter space in which efficient cooling can be achieved using only axial beams. In this case, the use of a perpendicular beam, whose parameters require careful optimization, is unnecessary.

A. KE_{\perp} cooling beyond the uncoupled approximation

Earlier, we found that the perpendicular kinetic energy was not cooled as well for crystals with larger β (see Fig. 7). This is, in fact, expected, and these kinetic energy cooling results are in agreement with the predictions of the theoretical treatment developed by Torrissi et al. in [43]. This model considers the dispersion of Doppler shifts sampled by the perpendicular cooling beam due to the ion crystal rotation and the finite waist of the laser beam. It predicts the post-cooling kinetic energy of 2D ion crystals given the values of key laser parameters, but has also been shown to accurately predict the

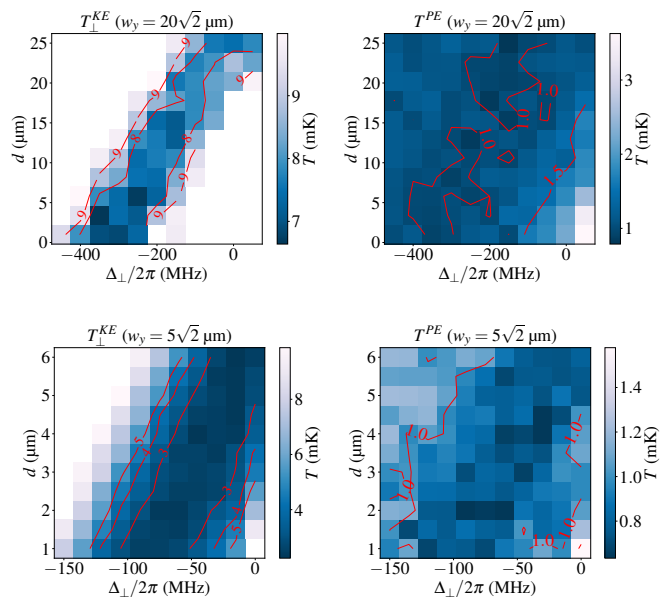


FIG. 8: The perpendicular kinetic energy and total potential energy of the large δ , $\omega_r = 2\pi \times 700$ kHz is shown. Each plot shows the final temperature after 16 ms of laser cooling as a function of perpendicular beam detuning, Δ_{\perp} and offset, d . The upper and lower plots are obtained using a perpendicular beam waist of $w_y = 20\sqrt{2} \mu\text{m}$ and $w_y = 5\sqrt{2} \mu\text{m}$, respectively. Note that the simulated (Δ_{\perp}, d) parameter space differs. The kinetic energy cooling dramatically improves by decreasing w_y , which suggests an experimental method to improve the cooling of larger β 3D crystals. The potential energy cooling also shows a slight improvement. White boxes represent simulations in which the temperature does not equilibrate after 16 ms.

temperatures of many 3D crystals [33]. Since the theoretical model does not account for f^z -coupling or resonant mode coupling, it is not guaranteed to produce correct cooling predictions in all 3D crystal regimes. However, since the cyclotron modes, which provide the dominant contribution to the perpendicular kinetic energy, remain almost entirely planar in a large parameter space, it is not surprising that the theory predictions hold for many 3D crystals. Nevertheless, as the crystal becomes increasingly prolate, effects of coupling appear.

In order to understand the limits of the Torrissi theory, we simulate the cooling of $N = 1000$ ion crystals with $\omega_r/2\pi \in \{400, 1000, 1600\}$ kHz. Here, we use $\delta = 0.104$ and $w_y = 20\sqrt{2} \mu\text{m}$. All other parameters have the same values as in the last section, except for Δ_{\perp} and d , which are once again chosen to minimize the predicted perpendicular kinetic energy. The KE_{\perp} values after 10 ms of laser cooling are shown in Fig. 9. Also shown are the corresponding theoretical temperatures obtained using the Torrissi model. This model does not account for planar anisotropy (i.e. nonzero δ). Therefore, to obtain the the-

oretical temperatures, we define the ion crystal's planar extent as the mean of its maximum and minimum planar extents. This approximation is not expected to significantly affect the results presented in this section.

We find excellent agreement between the simulated and theoretical results for $\omega_r = 2\pi \times 400$ kHz. At this rotation frequency, there is minimal coupling between planar and axial motion. As ω_r is increased, the Torrissi theory predicts that cooling of KE_{\perp} becomes less effective when the beam width is held constant, as seen in Fig. 9. However, at higher rotation frequencies, coupling effects ignored in the theoretical model lead to improved cooling in our simulations. This is seen at $\omega_r = 2\pi \times 1000$ kHz and $\omega_r = 2\pi \times 1600$ kHz, where the simulated kinetic energy is significantly lower than the theoretical predictions. Coupling effects become stronger as the rotation frequency increases, and we find that the simulated KE_{\perp} cooling is most effective at $\omega_r = 2\pi \times 1600$ kHz. In the absence of coupling, this crystal is predicted to exhibit the weakest cooling of KE_{\perp} . As such, MD simulations are essential to obtain accurate cooling results in the highly coupled regime. Finally, we note that the results for $\omega_r = 2\pi \times 1600$ kHz suggest that prolate ion crystals can quickly be cooled to temperatures of approximately 1 mK using a large range of laser parameters. This reduced sensitivity to laser parameters should allow excellent cooling to be achieved easily in experimental setups.

B. Cooling without perpendicular beam

As β is further increased, the axial component of the cyclotron modes continues to grow. In Fig. 10a, we plot f^z , as well as the mode spectra, for several $N = 1000$ ion crystals with $\omega_r/2\pi$ between 1 MHz and 1.9 MHz (using $\delta = 0.173$). The remaining trap and axial beam parameters are the same as in the previous sections. Within this parameter space, the perpendicular cooling beam becomes unnecessary to achieve milliKelvin temperatures. In Fig. 10b, we plot the cooling of the kinetic and potential energy of these high β crystals when only the axial cooling beams are applied. At $\omega_r = 2\pi \times 1$ MHz, the axial kinetic and potential energies are rapidly cooled to $\lesssim 1$ mK, but the perpendicular kinetic energy is not cooled below its initial temperature of 10 mK. However, as ω_r increases, the perpendicular kinetic energy is cooled much more effectively by the axial beams. At $\omega_r/2\pi = 1.6$ MHz and 1.9 MHz, KE_{\perp} reaches < 1 mK within a few milliseconds of cooling.

While the perpendicular beam is primarily responsible for cooling the cyclotron motion in lower β crystals, the axial beams can effectively cool these modes in large β crystals, often to even lower temperatures. Therefore, the use of such crystals could eliminate the need to optimize the perpendicular beam parameters and experimentally configure the perpendicular beam. As such, prolate crystals may be attractive platforms for future quantum

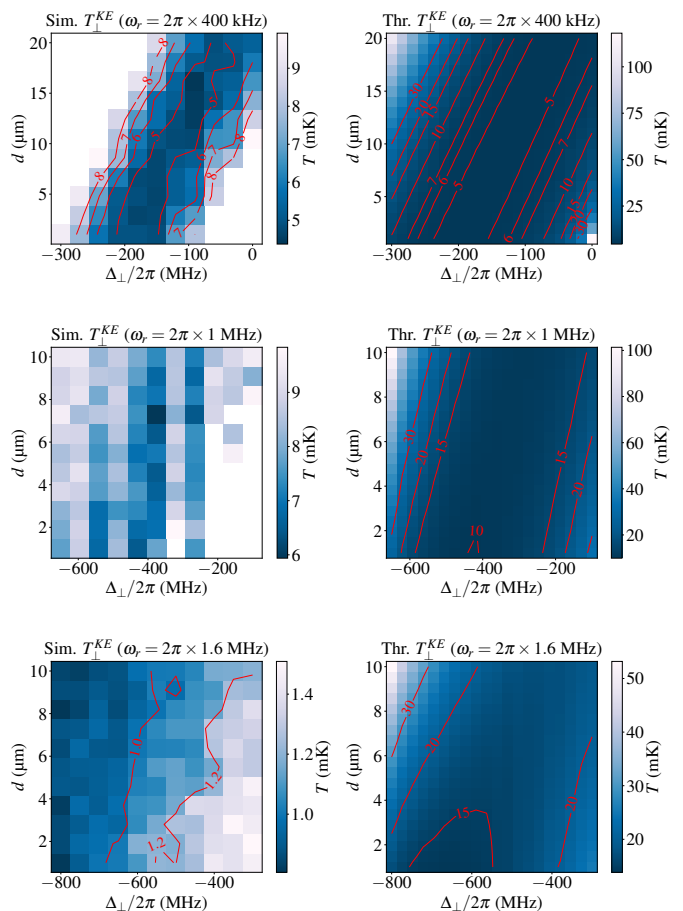


FIG. 9: The simulated perpendicular kinetic energy after laser cooling is compared to theoretical predictions for three $N = 1000$ ion crystals with different values of ω_r . Our simulations (left-hand figures) use 10 ms of laser cooling, and the theoretical predictions (right-hand figures) are obtained using the model from [43], which has been extended to 3D crystals in [33]. The rows of figures correspond to $\omega_r/2\pi = 400$ kHz, 1 MHz, and 1.6 MHz, respectively. The theoretical model does not account for cooling of the cyclotron motion by the axial laser beam, and is therefore not guaranteed to produce reliable results for 3D crystals. Still, we see that the simulated and predicted temperatures agree quite well for lower β crystals, such as the $\omega_r = 2\pi \times 400$ kHz one. As ω_r increases, the theoretical treatment predicts increased perpendicular kinetic energies. However, at $\omega_r = 2\pi \times 1$ MHz, the simulated kinetic energies are significantly smaller than these predictions. We attribute this result to the effect of increased coupling in this regime. This behavior is amplified in the $\omega_r = 2\pi \times 1.6$ MHz case, where we see cooling to below 1 mK throughout a large parameter space.

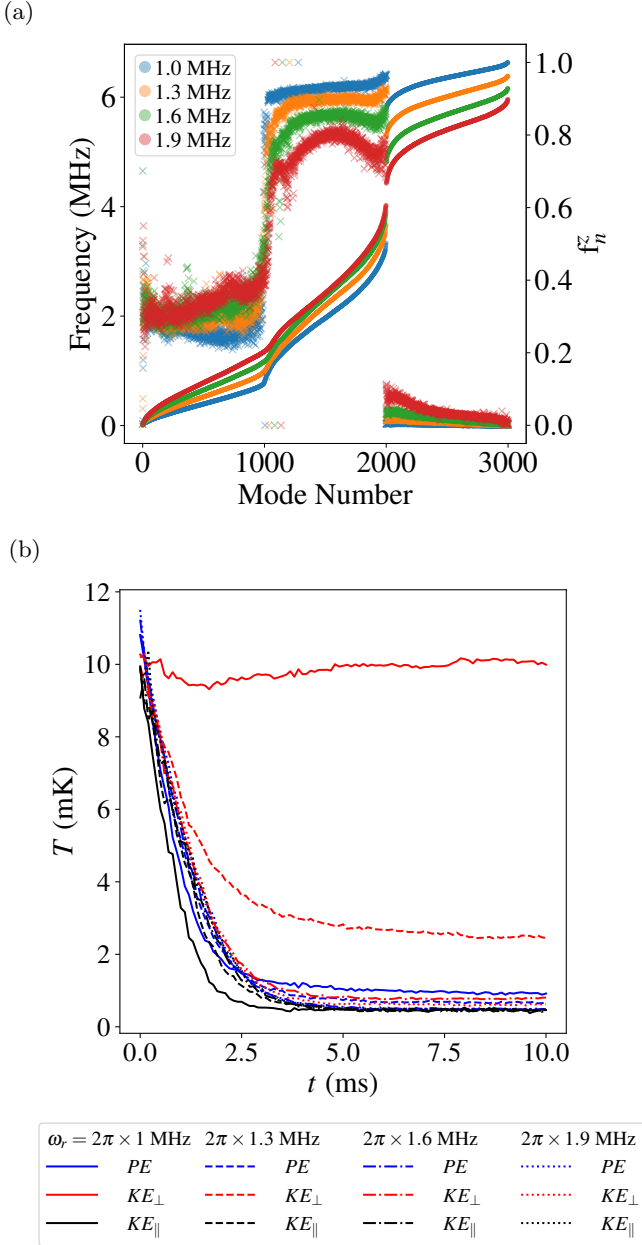


FIG. 10: (a) Mode spectra and mode f^z values for several high β crystals with different values of $\omega_r/2\pi$. The cyclotron modes gain a significant axial component. (b) Cooling curves for these crystals using only axial beams. In all cases shown here, potential and axial kinetic energies are reduced to temperatures of < 1 mK within several milliseconds. For the larger values of ω_r , the perpendicular kinetic energy is also cooled to < 1 mK.

science experiments.

V. SCALING UP TO LARGER ION NUMBER

In order to develop transformative quantum sensing applications with 3D crystals, it will be desirable to trap larger ion crystals of $\sim 10^5 - 10^6$ ions. With this experimental goal in mind, our MD code has been designed for numerical efficiency when simulating large N crystals. In this section, we carry out a preliminary study of laser cooling of a $N = 10^5$ ion crystal.

Certain methods from the preceding sections must be modified when studying such large crystals. First, it is prohibitively inefficient to use line-search based energy minimization techniques like BFGS to find equilibrium configurations for large N . For this reason, we have implemented a dynamical minimization technique, which utilizes numerical damping, to relax a cloud of ions with randomized initial positions to a local equilibrium configuration. This method relies on evolving the ions according to the Penning trap equations of motion while removing a small fraction of each ion's velocity in the rotating frame at each timestep. In order to accelerate the damping process, we modify our MD code to remove the high frequency cyclotron motion which limits the speed of numerical damping. First, we evolve the ions according to the equations of motion in the rotating frame, rather than those in the lab frame. The coordinate transformation to the rotating frame is given by

$$\begin{pmatrix} x_r \\ y_r \end{pmatrix} = \begin{pmatrix} \cos(\omega_r t) & -\sin(\omega_r t) \\ \sin(\omega_r t) & \cos(\omega_r t) \end{pmatrix} \begin{pmatrix} x \\ y \end{pmatrix}. \quad (18)$$

In both the lab frame and rotating frame, the magnetic field produces terms in the system's Hamiltonian which are proportional to mixed position-velocity products like $\dot{x}y_r$. Our MD cooling simulation employs a cyclotronic integrator [45] to account for the resulting motion. However, in our damping algorithm, we ignore these terms since the ion velocities vanish at equilibrium. This is equivalent to setting the effective magnetic field in the rotating frame equal to zero [37] and evolving the ions in a purely electrostatic potential. The potential energy is explicitly given by

$$\begin{aligned} \phi_r(\{\mathbf{x}_n\}) = & \sum_j \left[\frac{1}{2} m \omega_z^2 z_j^2 \right. \\ & - \frac{1}{2} m (\omega_r^2 - \omega_c \omega_r + \frac{1}{2} \omega_z^2) (x_j^2 + y_j^2) \\ & \left. + \frac{1}{2} q k_z \delta(x_j^2 - y_j^2) + \frac{kq^2}{2} \sum_{k \neq j} \frac{1}{r_{jk}} \right], \end{aligned} \quad (19)$$

where we have dropped the 'r' subscript on the ion coordinates for simplicity. The previously described simplification removes cyclotron motion, thereby changing the ion

dynamics. However, it does not affect the potential energy landscape of the system. At each timestep ($\Delta t = 1$ ns), we reduce the kinetic energy of each ion by a factor of 10^{-4} . In general, slower energy reduction causes the crystal to relax into lower energy local equilibrium states, but also requires longer damping simulations. We note briefly that other dynamical energy minimization techniques have been developed for large ion crystals, including the simulation of guiding center motion [46] and the implementation of Nose-Hoover thermostats [47].

Initializing the crystal's potential energy using an Metropolis-Hastings algorithm becomes extremely slow for large N . Therefore, we implement an initialization routine based on Langevin dynamics in the rotating frame. Specifically, starting from the equilibrium configuration, we evolve the system according to the Langevin equation

$$m \frac{d^2 \mathbf{x}_i}{dt^2} = \mathbf{F}_i - \gamma \dot{\mathbf{x}}_i + \sqrt{2\gamma k_B T} \boldsymbol{\xi}_i(t). \quad (20)$$

Here, T is set to the desired initial temperature, $\mathbf{F}_i = -q\nabla\phi_r(\mathbf{x}_i)$ is the force on ion i (in the rotating frame), and γ is the damping factor. The Gaussian noise term, $\boldsymbol{\xi}_i(t) = \xi_{i,x}(t)\hat{\mathbf{x}} + \xi_{i,y}(t)\hat{\mathbf{y}} + \xi_{i,z}(t)\hat{\mathbf{z}}$, satisfies the correlation function $\langle \xi_{i,\alpha}(t)\xi_{i,\beta}(t') \rangle = \delta_{\alpha,\beta}\delta(t-t')$. The damping algorithm described earlier is equivalent to Eq. (20) with $T = 0$. We use a velocity Verlet algorithm to integrate Eq. (20) in time. Since the crystal is initialized in a harmonic potential (Eq. (19)), the kinetic and potential energies are excited equally. By comparing the potential energies of an $N = 10^5$ ion crystal obtained using the Langevin thermostat and the corresponding equilibrium crystal found using numerical damping, we verify that the potential energy is initialized at approximately 10 mK. However, the exact potential energy difference between the crystals is slightly less than 10 mK. This is likely because the damping algorithm is unable to find the global energy-minimizing ion configuration for large crystals, leading to an ‘equilibrium’ potential energy which is small, but nonzero. For this reason, we define the potential energy of the Langevin-initialized crystal as $T = 10$ mK when plotting cooling results.

Following this scheme, we prepare a $N = 10^5$ ion crystal with the following trap parameters: $B = 4.4588$ T, $\omega_z = 2\pi \times 1.59$ MHz, $\omega_r = 2\pi \times 1.9$ MHz, and $\delta = 0.173$. The equilibrium ion configuration is shown in Fig. 11a. The concentric shell structure which characterizes ellipsoidal crystals [25] is evident, although the shells appear smeared out due to the large value of δ which creates planar anisotropy. We initialize the crystal at 10 mK using 10^5 timesteps of the Langevin thermostat and then simulate Doppler cooling. In Fig. 11b, we plot the resulting cooling curves. Since the simulation time increases approximately linearly with ion number, it is helpful to consider increasing the simulation timestep. Increasing the timestep to 2 ns, in which case $\omega_c\Delta t = 0.095$, leads to smooth cooling curves, as shown in Fig. 11b.

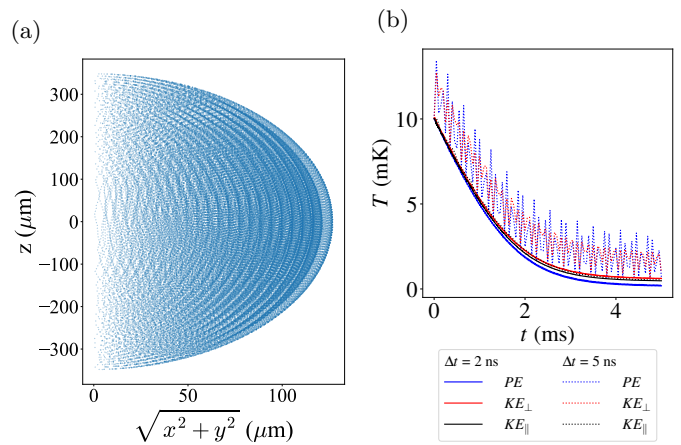


FIG. 11: (a) Local equilibrium ion configuration of an $N = 10^5$ crystal with $B = 4.4588$ T, $\omega_z = 2\pi \times 1.59$ MHz, $\omega_r = 2\pi \times 1.9$ MHz, and $\delta = 0.173$ (b) Cooling of the crystal's energy using only axial beams. Using $\Delta t = 2$ ns, all energies are cooled to below 1 mK within 5 ms, similar to the results seen in Fig. 10. The potential energy configuration corresponding to 0 mK is found using numerical damping, as described in the text. Here, laser cooling over 5 ms causes the potential energy to be cooled below this level. We do not carry out a reminimization here, as was done for previous simulations.

However, further increasing the timestep to $\Delta t = 5$ ns ($\omega_c\Delta t = 0.24$) leads to numerical instabilities and results in noisier cooling curves. Based on the $\Delta t = 2$ ns simulation, we find that all energies are cooled to < 1 mK within 5 ms. Note that the potential energy reaches negative values because we have not reminimized the crystal after cooling.

VI. CONCLUSION

In this work, we have developed computational tools to efficiently simulate dynamics of 3D crystals with up to 10^5 ions (see section V). Using MD simulations, we have characterized Doppler laser cooling of 3D crystals, providing results that will guide experimental efforts to prepare large ion crystals at low temperatures. By studying the normal mode structure of 3D crystals, we have shown that cooling generally improves when modes gain an axial component. In particular, PE (KE_{\perp}) cooling improves when the $\mathbf{E} \times \mathbf{B}$ (cyclotron) modes have larger values of f^z . Cooling can be further enhanced by tuning parameters like the rotating wall strength and the perpendicular beam waist. Interestingly, we have discovered that, in the high β regime, it should be possible to quickly cool the crystal energies to below 1 mK without the need for a perpendicular cooling beam. This suggests a way to achieve enhanced cooling in 3D crystals

while simultaneously simplifying the experimental setup. We note that as the rotation frequency increases to near the Brillouin limit ($\omega_r = \omega_c/2$), cooling may be degraded due to anomalous heating effects. Previous experiments with nonneutral plasmas have observed increased heating at large rotating wall frequencies due to slipping of the plasma relative to the field [48]. This may provide a practical limit on the range of feasible ω_r values.

Future studies may aim to further investigate the mechanism responsible for improved cooling in 3D crystals. In particular, by utilizing a linearized version of the MD code, in which mode coupling vanishes, one could determine the relative effects of (1) the narrowing frequency gap between mode branches and (2) the increasing values of f^z in ‘planar’ modes. In future work, we will also aim to simulate electromagnetically-induced transparency (EIT) cooling of trapped ion crystals, which results in near-ground state cooling of the axial modes [17, 26]. In particular, we will investigate if EIT cooling can result in sub-Doppler cooling of $\mathbf{E} \times \mathbf{B}$ and cyclotron modes in 3D crystals.

ACKNOWLEDGMENTS

The authors thank Dietrich Leibfried, Diep Nguyen, and Yuan Shi for reading the manuscript and providing insightful feedback. We also appreciate helpful discussions with Bryce Bullock and Jennifer Lilieholm. J.Z, W.J, and S.E.P. were supported by U.S. Department of Energy grant DE-SC0020393. A.S. acknowledges support by the Department of Science and Technology, Govt. of India through the INSPIRE Faculty Award (DST/INSPIRE/04/2023/001486), by the Anusandhan National Research Foundation (ANRF), Govt. of India through the Prime Minister’s Early Career Research Grant (PMECRG) (ANRF/ECRG/2024/001160) and by IIT Madras through the New Faculty Initiation Grant (NFIG). A.L.C. and J.J.B acknowledge support from AFOSR grant FA9550-25-1-0080 and from the DOE NQIS Research Center, Quantum System Accelerator.

-
- [1] J. W. Britton, B. C. Sawyer, A. C. Keith, C.-C. J. Wang, J. K. Freericks, H. Uys, M. J. Biercuk, and J. J. Bollinger, Engineered two-dimensional Ising interactions in a trapped-ion quantum simulator with hundreds of spins, *Nature* **484**, 489 (2012).
- [2] A. Safavi-Naini, R. J. Lewis-Swan, J. G. Bohnet, M. Gärttner, K. A. Gilmore, J. E. Jordan, J. Cohn, J. K. Freericks, A. M. Rey, and J. J. Bollinger, Verification of a many-ion simulator of the Dicke model through slow quenches across a phase transition, *Phys. Rev. Lett.* **121**, 040503 (2018).
- [3] J. Cohn, A. Safavi-Naini, R. J. Lewis-Swan, J. G. Bohnet, M. Gärttner, K. A. Gilmore, J. E. Jordan, A. M. Rey, J. J. Bollinger, and J. K. Freericks, Bang-bang shortcut to adiabaticity in the Dicke model as realized in a Penning trap experiment, *New Journal of Physics* **20**, 055013 (2018).
- [4] A. Shankar, E. A. Yuzbashyan, V. Gurarie, P. Zoller, J. J. Bollinger, and A. M. Rey, Simulating dynamical phases of chiral $p + ip$ superconductors with a trapped ion magnet, *PRX Quantum* **3**, 040324 (2022).
- [5] M. Qiao, Z. Cai, Y. Wang, B. Du, N. Jin, W. Chen, P. Wang, C. Luan, E. Gao, X. Sun, H. Tian, J. Zhang, and K. Kim, arXiv (2022), arXiv:2204.07283.
- [6] J. H. Pham, J. Y. Z. Jee, A. Rischka, M. J. Biercuk, and R. N. Wolf, In situ-tunable spin-spin interactions in a Penning trap with in-bore optomechanics, *Adv. Quantum Technol.* **7**, 2400086 (2024), arXiv:2401.17742 [quant-ph].
- [7] B. Swingle, G. Bentsen, M. Schleier-Smith, and P. Hayden, Measuring the scrambling of quantum information, *Phys. Rev. A* **94**, 040302 (2016).
- [8] M. Gärttner, J. G. Bohnet, A. Safavi-Naini, M. L. Wall, J. J. Bollinger, and A. M. Rey, Measuring out-of-time-order correlations and multiple quantum spectra in a trapped ion quantum magnet, *Nature Phys.* **13**, 781 (2017), arXiv:1608.08938 [quant-ph].
- [9] J. G. Bohnet, B. C. Sawyer, J. W. Britton, M. L. Wall, A. M. Rey, M. Foss-Feig, and J. J. Bollinger, Quantum spin dynamics and entanglement generation with hundreds of trapped ions, *Science* **352**, 1297 (2016).
- [10] L. Pezzè, A. Smerzi, M. K. Oberthaler, R. Schmied, and P. Treutlein, Quantum metrology with nonclassical states of atomic ensembles, *Rev. Mod. Phys.* **90**, 035005 (2018).
- [11] K. A. Gilmore, J. G. Bohnet, B. C. Sawyer, J. W. Britton, and J. J. Bollinger, Amplitude sensing below the zero-point fluctuations with a two-dimensional trapped-ion mechanical oscillator, *Phys. Rev. Lett.* **118**, 263602 (2017).
- [12] M. Affolter, K. A. Gilmore, J. E. Jordan, and J. J. Bollinger, Phase-coherent sensing of the center-of-mass motion of trapped-ion crystals, *Phys. Rev. A* **102**, 052609 (2020).
- [13] K. A. Gilmore, M. Affolter, R. J. Lewis-Swan, D. Barberena, E. Jordan, A. M. Rey, and J. J. Bollinger, Quantum-enhanced sensing of displacements and electric fields with two-dimensional trapped-ion crystals, *Science* **373**, 673 (2021).
- [14] F. Toscano, D. A. R. Dalvit, L. Davidovich, and W. H. Zurek, Sub-Planck phase-space structures and Heisenberg-limited measurements, *Phys. Rev. A* **73**, 023803 (2006).
- [15] R. N. Wolf, J. H. Pham, J. Y. Z. Jee, A. Rischka, and M. J. Biercuk, Efficient site-resolved imaging and spin-state detection in dynamic two-dimensional ion crystals, *Phys. Rev. Appl.* **21**, 054067 (2024).
- [16] B. J. McMahon, K. R. Brown, C. D. Herold, and B. C. Sawyer, Individual-ion addressing and readout in a Penning trap, *Phys. Rev. Lett.* **133**, 173201 (2024).
- [17] D. Kiesenhofer, H. Hainzer, A. Zhdanov, P. C. Holz, M. Bock, T. Ollikainen, and C. F. Roos, Controlling two-dimensional Coulomb crystals of more than 100 ions in a monolithic radio-frequency trap, *PRX Quantum* **4**, 020317 (2023).

- [18] S. A. Guo et al., A site-resolved two-dimensional quantum simulator with hundreds of trapped ions, *Nature* **630**, 613 (2024), arXiv:2311.17163 [quant-ph].
- [19] S. Hawaldar, P. Shahi, A. L. Carter, A. M. Rey, J. J. Bollinger, and A. Shankar, Bilayer crystals of trapped ions for quantum information processing, *Phys. Rev. X* **14**, 031030 (2024).
- [20] H. N. Hausser, J. Keller, T. Nordmann, N. M. Bhatt, J. Kiethe, H. Liu, I. M. Richter, M. von Boehn, J. Rahm, S. Weyers, E. Benkler, B. Lipphardt, S. Dörscher, K. Stahl, J. Klose, C. Lisdat, M. Filzinger, N. Hunte- mann, E. Peik, and T. E. Mehlstäubler, $^{115}\text{In}^+ - ^{172}\text{Yb}^+$ Coulomb crystal clock with 2.5×10^{-18} systematic uncertainty, *Phys. Rev. Lett.* **134**, 023201 (2025).
- [21] D. R. Leibbrandt, S. G. Porsev, C. Cheung, and M. S. Safronova, Prospects of a thousand-ion Sn^{2+} Coulomb-crystal clock with sub- 10^{-19} inaccuracy, *Nature Commun.* **15**, 5663 (2024), arXiv:2205.15484 [physics.atom-ph].
- [22] W. M. Itano, J. J. Bollinger, J. N. Tan, B. Jelenković, X.-P. Huang, and D. J. Wineland, Bragg diffraction from crystallized ion plasmas, *Science* **279**, 686 (1998).
- [23] W. M. Itano, L. R. Brewer, D. J. Larson, and D. J. Wineland, Perpendicular laser cooling of a rotating ion plasma in a Penning trap, *Phys. Rev. A* **38**, 5698 (1988).
- [24] M. Drewsen, C. Brodersen, L. Hornekær, J. S. Hangst, and J. P. Schiffer, Large ion crystals in a linear Paul trap, *Phys. Rev. Lett.* **81**, 2878 (1998).
- [25] D. H. E. Dubin and T. M. O’Neil, Trapped nonneutral plasmas, liquids, and crystals (the thermal equilibrium states), *Rev. Mod. Phys.* **71**, 87 (1999).
- [26] E. Jordan, K. A. Gilmore, A. Shankar, A. Safavi-Naini, J. G. Bohnet, M. J. Holland, and J. J. Bollinger, Near ground-state cooling of two-dimensional trapped-ion crystals with more than 100 ions, *Phys. Rev. Lett.* **122**, 053603 (2019).
- [27] A. Shankar, C. Tang, M. Affolter, K. Gilmore, D. H. E. Dubin, S. Parker, M. J. Holland, and J. J. Bollinger, Broadening of the drumhead-mode spectrum due to in-plane thermal fluctuations of two-dimensional trapped ion crystals in a Penning trap, *Phys. Rev. A* **102**, 053106 (2020).
- [28] W. Johnson, A. Shankar, J. Zaris, J. J. Bollinger, and S. E. Parker, Rapid cooling of the in-plane motion of two-dimensional ion crystals in a Penning trap to millikelvin temperatures, *Phys. Rev. A* **109**, L021102 (2024).
- [29] W. Johnson, B. Bullock, A. Shankar, J. Zaris, J. J. Bollinger, and S. E. Parker, Adiabatic cooling of planar motion in a Penning-trap ion crystal to sub-millikelvin temperatures, *Phys. Rev. A* **112**, 063110 (2025).
- [30] A. Mortensen, E. Nielsen, T. Matthey, and M. Drewsen, Observation of three-dimensional long-range order in small ion Coulomb crystals in an rf trap, *Phys. Rev. Lett.* **96**, 103001 (2006).
- [31] C. Tang, D. Meiser, J. J. Bollinger, and S. E. Parker, First principles simulation of ultracold ion crystals in a Penning trap with Doppler cooling and a rotating wall potential, *Physics of Plasmas* **26**, 073504 (2019).
- [32] A. Poindron, J. Pedregosa-Gutierrez, and C. Champenois, Thermal bistability in laser-cooled trapped ions, *Phys. Rev. A* **108**, 013109 (2023).
- [33] J. Zaris, W. Johnson, A. Shankar, J. J. Bollinger, and S. E. Parker, Numerical simulations of three-dimensional ion crystal dynamics in a Penning trap using the fast multipole method, *Journal of Plasma Physics* **91**, E53 (2025).
- [34] L. Greengard and V. Rokhlin, A fast algorithm for particle simulations, *Journal of Computational Physics* **73**, 325 (1987).
- [35] L. Greengard and V. Rokhlin, A new version of the fast multipole method for the Laplace equation in three dimensions, *Acta Numerica* **6**, 229–269 (1997).
- [36] H. Cheng, L. Greengard, and V. Rokhlin, A fast adaptive multipole algorithm in three dimensions, *Journal of Computational Physics* **155**, 468 (1999).
- [37] C.-C. J. Wang, A. C. Keith, and J. K. Freericks, Phonon-mediated quantum spin simulator employing a planar ionic crystal in a Penning trap, *Phys. Rev. A* **87**, 013422 (2013).
- [38] D. H. E. Dubin, Normal modes, rotational inertia, and thermal fluctuations of trapped ion crystals, *Physics of Plasmas* **27**, 102107 (2020).
- [39] S. Jain, J. Alonso, M. Grau, and J. P. Home, Scalable arrays of micro-Penning traps for quantum computing and simulation, *Phys. Rev. X* **10**, 031027 (2020).
- [40] D. H. E. Dubin, Theory of structural phase transitions in a trapped Coulomb crystal, *Phys. Rev. Lett.* **71**, 2753 (1993).
- [41] D. H. E. Dubin, Theory of electrostatic fluid modes in a cold spheroidal non-neutral plasma, *Phys. Rev. Lett.* **66**, 2076 (1991).
- [42] A. W. Trivelpiece and R. W. Gould, Space charge waves in cylindrical plasma columns, *Journal of Applied Physics* **30**, 1784 (1959).
- [43] S. B. Torrisi, J. W. Britton, J. G. Bohnet, and J. J. Bollinger, Perpendicular laser cooling with a rotating-wall potential in a Penning trap, *Phys. Rev. A* **93**, 043421 (2016).
- [44] T. B. Mitchell, J. J. Bollinger, W. M. Itano, and D. H. E. Dubin, Stick-slip dynamics of a stressed ion crystal, *Phys. Rev. Lett.* **87**, 183001 (2001).
- [45] L. Patacchini and I. Hutchinson, Explicit time-reversible orbit integration in particle in cell codes with static homogeneous magnetic field, *Journal of Computational Physics* **228**, 2604 (2009).
- [46] D. H. E. Dubin and T. M. O’Neil, Computer simulation of ion clouds in a Penning trap, *Phys. Rev. Lett.* **60**, 511 (1988).
- [47] H. Totsuji, T. Kishimoto, C. Totsuji, and K. Tsuruta, Competition between two forms of ordering in finite Coulomb clusters, *Phys. Rev. Lett.* **88**, 125002 (2002).
- [48] X.-P. Huang, F. Anderegg, E. M. Hollmann, C. F. Driscoll, and T. M. O’Neil, Steady-state confinement of non-neutral plasmas by rotating electric fields, *Phys. Rev. Lett.* **78**, 875 (1997).